ADVANCED ENERGY MATERIALS
www.advenergymat.de

Improving Ca-ion Storage Dynamic and Stability by Interlayer Engineering and Mn-dissolution Limitation Based on Robust MnO_2@PANI Hybrid Cathode

Chunli Zuo, Feiyang Chao, Ming Li, Yuhang Dai, Junjun Wang, Fangyu Xiong, Yalong Jiang,* and Qinyou An**

Rechargeable Ca-ion batteries (CIBs) have attracted great interest due to potentially high output voltage and abundant calcium resources. Among various cathode materials, manganese oxides with high theoretical capacity and low cost are suitable as strong candidates for rechargeable CIBs. However, the dissolution of manganese and the strong electrostatic interactions between Ca^{2+} and host materials result in inferior cycle stability and poor rate performance. Herein, a MnO_2-polyaniline (PANI) hybrid cathode with both PANI intercalation and coating is developed to solve the above problems. The intercalation of PANI can expand the interlayer spacing and effectively buffer the local electrostatic interaction for facile Ca^{2+} diffusion. Meanwhile, the density functional theory (DFT) calculations prove that the PANI coating inhibits manganese dissolution by forming strong Mn-N bonds to enhance the structural integrity of MnO_2. Benefitting from the above, the MnO_2-PANI (MnO_2-P) cathode delivers high capacity (150 mAh g^{-1} at 0.1 A g^{-1}), excellent rate performance (120 mAh g^{-1} at 1 A g^{-1}) and long-term cycling stability (5000 cycles). The organic-inorganic hybrid desig provides a new strategy for developing high performance CIBs cathode materials.

1. Introduction

In recent years, with the increasing demands for electric vehicles and fixed energy storage systems, it is urgent to search new energy storage technologies with lower cost, higher energy density and longer lifespan.[1] Multivalent-ion batteries based on the multi-electron reaction can provide higher theoretical energy density .[2] Ca-ion batteries (CIBs) are attracting a great deal of attention due to the low standard potential (−2.87 V vs SHE) of Ca metal,[3] low polarization intensity of Ca^{2+}[4] and high abundance of Ca resources. Nevertheless, the development of CIBs is confined by poor rate performance of the current cathode materials due to the slow migration kinetics of Ca^{2+} ions and the structural damage of host materials stemming from the large size of Ca^{2+} ions.[5] Therefore, it is very important to develop high-performance cathode materials to accelerate the development of CIBs.

Manganese dioxide (MnO_2) have been identified as an promising cathode material for various multivalent-ion batteries due to its diverse crystal structures, nontoxic, high energy density and good economic benefits.[6] Unfortunately, the research about MnO_2 as cathode materials for CIBs is rarely reported. Our previous research has first reported four types of MnO_2 polymorphs (α, β, γ, and δ-phase) as CIBs cathode material, wherein δ-MnO_2 exhibits the best electrochemical performance due to the higher Ca-ion diffusivity of δ-MnO_2.[7] Nevertheless, the δ-MnO_2 still suffers from poor cycle life and rate performance. In terms of the

C. Zuo, M. Li, Y. Dai, J. Wang, F. Xiong, Y. Jiang, Q. An
State Key Laboratory of Advanced Technology for Materials Synthesis and Processing
Wuhan University of Technology
Wuhan 430070, P. R. China
E-mail: xfy@whut.edu.cn; jyl504@whut.edu.cn; anqinyou86@whut.edu.cn

F. Chao
Hubei Provincial Key Laboratory of Green Materials for Light Industry
School of Materials and Chemical Engineering
Hubei University of Technology
Wuhan 430068, P. R. China

Y. Jiang
State Key Laboratory of New Textile Materials and Advanced Processing Technologies
Wuhan Textile University
Wuhan 430200, P. R. China

Q. An
Wuhan University of Technology (Xiangyang Demonstration Zone)
Xiangyang 441000, P. R. China

The ORCID identification number(s) for the author(s) of this article can be found under https://doi.org/10.1002/aenm.202301014

DOI: 10.1002/aenm.202301014

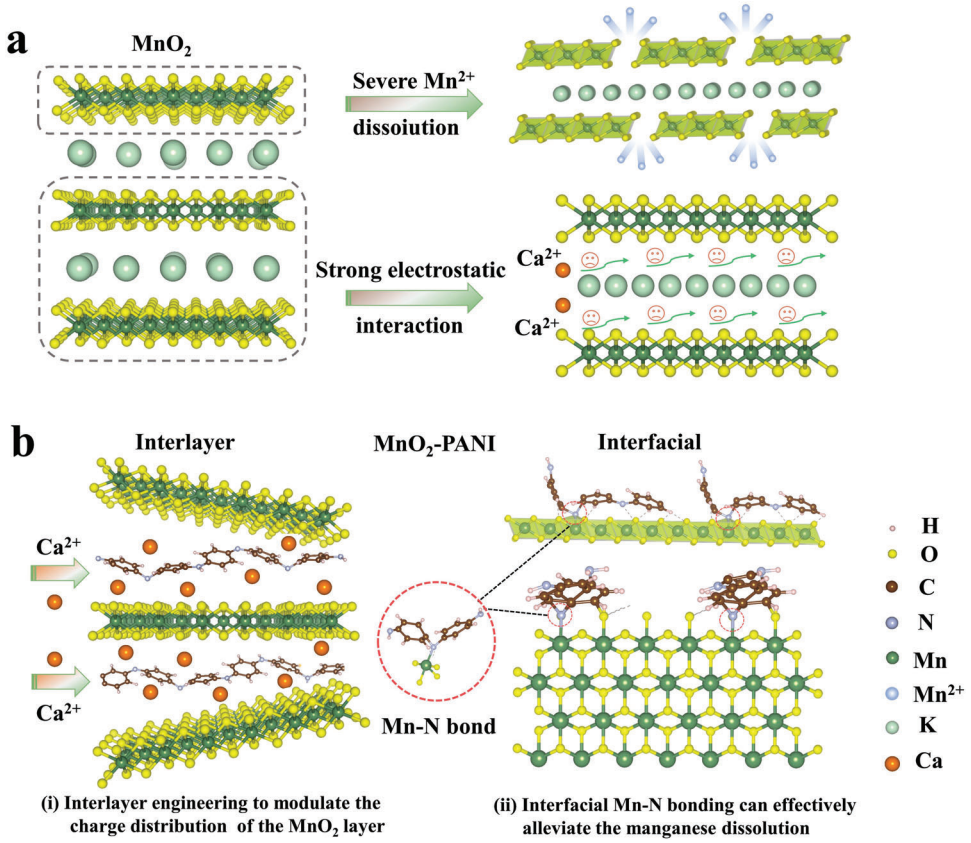

Figure 1. Schematic illustration of the proposed strategy. a) the pristine MnO_2 suffers from severe dissolution of Mn^{2+} due to the disproportionation reaction of Mn^{3+} and the strong electrostatic reaction between Ca^{2+} ions and host material results in slow diffusion dynamics. b) Interlayer engineering and interface design can effectively promote ion diffusion and inhibit Mn dissolution.

reaction mechanism of batteries, this is due to manganese-based materials suffer from the disproportional reaction of Mn^{3+} during electrochemical process, leading to manganese dissolution and structural degradation.[8] Furthermore, the strong electrostatic interaction between Ca^{2+} ions and manganese oxide layer hinders the diffusion dynamics,[9] resulting in the poor rate performance (**Figure 1**a). Therefore, it is a very important challenge to explore effective strategies to enlarge the interlayer space, suppress the cathode dissolution, and shield the electrostatic interaction of guest ion for the MnO_2. The organic-inorganic hybrid structure has the characteristics of large interlayer space, multiple interfaces, and charge redistribution between adjacent layers, displaying exciting electrochemical performances in other multivalent ion batteries.[10] Whereas, this remarkable structure as cathode materials for CIBs has not been report yet.

Herein, we reported a strategy to comprehensively improve the Ca-ion storage dynamic and stability of MnO_2 cathode material for CIBs by introducing polyaniline (PANI) and PANI coating layer. The intercalation of PANI not only enlarges the interlayer spacing but also shields the electrostatic interaction between Ca^{2+} ions and MnO_2 host, facilitating Ca^{2+} diffusion (Figure 1b). Meanwhile, the Mn-N bonds are formed at the interface between MnO_2 and PANI coating, which can effectively inhibit the dissolution of manganese. In addition, the results of density functioncal theory (DFT) calculation show that electron delocalization on PANI chain reduces the electron interaction between Ca^{2+} ion and MnO_2, thereby promoting the extraction/insertion process of Ca^{2+}. Benefitting from the above features, theMnO_2 with PANI intercalation and coating (MnO_2-P) cathode exhibits superior rate performance and cyclic stability compared to the MnO_2. To the best of our knowledge, the MnO_2-P delivers a long cycle life of 5000 cycles, which is superior to the all previously reported oxides as cathode materials for CIBs. Meanwhile, in situ X–Ray Diffracion (XRD) and ex situ characterizations show that the (de)intercalation mechanism of Ca^{2+} in MnO_2-P is a single-phase solid solution reaction.

2. Results and Discussion

The synthsis of MnO_2-P organic-inorganic hybrid structure is depicted in **Figure 2**a. When the MnO_2 and polyaniline are mixed, PANI is inserted into the interlayer of manganese dioxide while forming a PANI coating on the surface of manganese dioxide, thus forming a hybrid structure (MnO_2-P). The XRD pattern (Figure 2b) displays that the as-synthesized MnO_2 is birnessite MnO2 (JCPDS card No. 087–1497) without any impurities.[1b] Compared with the pristine MnO_2, the layer spacing increased from 0.70 to 0.72 nm after the insertion of PANI. The associated energy dispersive spectroscopy (EDS) line-scan elemental distribution profiles indicate that the MnO_2-P microsheet has

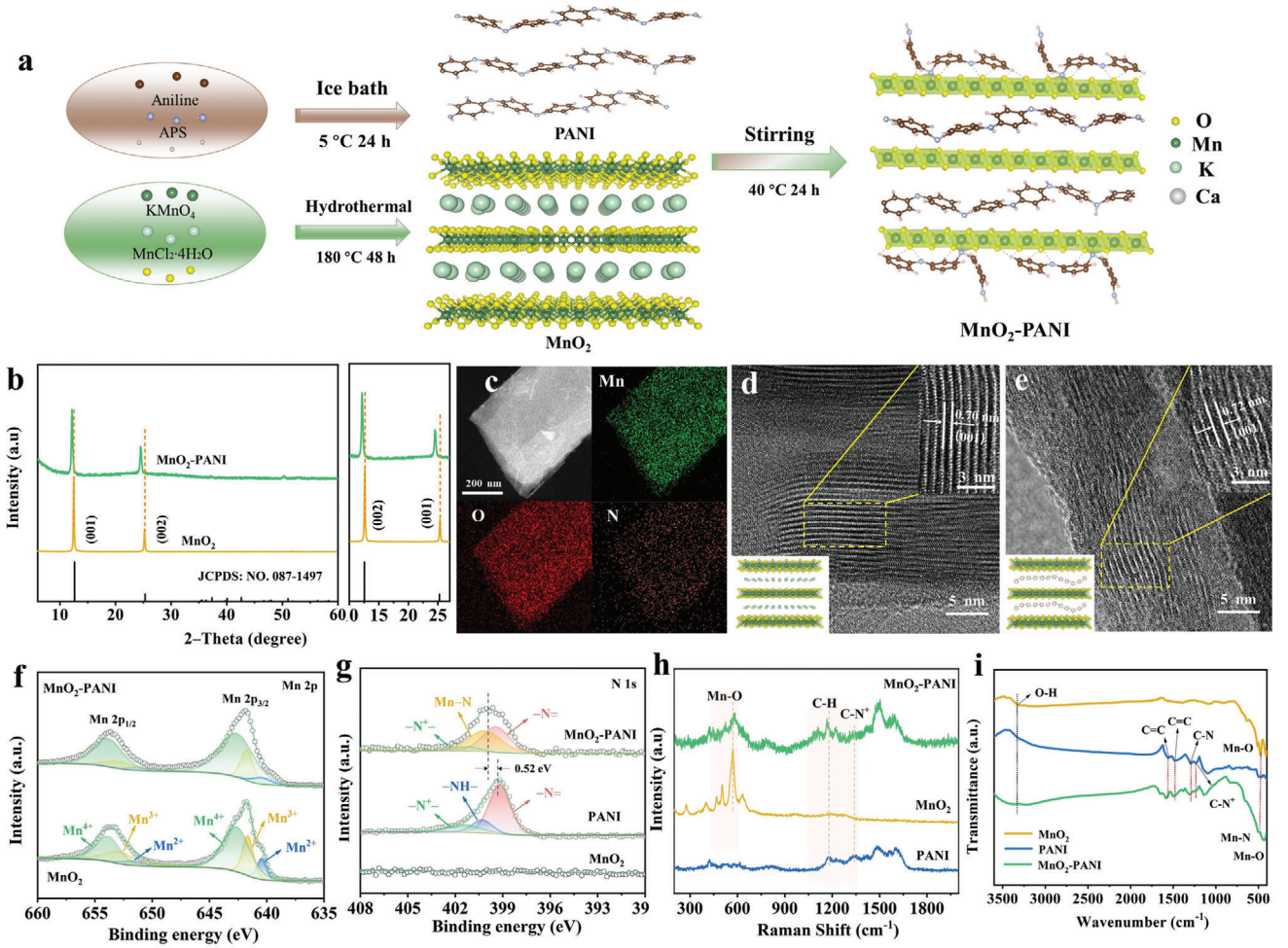

Figure 2. a) Schematic synthesis of the MnO_2-P organic-inorganic nanosheets. b) XRD patterns of pristine MnO_2, MnO_2-P . c) TEM-EDS mapping of MnO_2-P. d,e,f) HRTEM images and Mn 2p XPS spectra of MnO_2 and MnO_2-P. g) N 1s XPS spectra, h) Raman spectra, and i) FTIR spectra of PANI, MnO_2 and MnO_2-P.

a smooth surface and the Mn, O, and N atoms are evenly distributed. This further indicates the insertion of PANI (Figure S1, Supporting Information). To further demonstrate that interlayer changes can be attributed to the insertion of PANI, rather than just the removal of potassium ions, we characterized the MnO_2 after electrochemical depotassiation. The electrochemical depotassiation process of the cathode electrode of MnO_2 was performed in a MnO_2//AC cell. The inductively coupled plasma optical emission spectrometer (ICP–OES) test results (Table S1, Supporting Information) show that the atomic ratio of K:Mn in depotassiatedMnO_2 (D-MnO_2) is 0.15:1, which indicates that potassium ions in MnO_2 are partially removed during the charging process. In addition, the XRD pattern (Figure S2, Supporting Information) displays that the peaks of D-MnO_2 corresponding to the (001) and (002) planes shift to a lower angle compared with the MnO_2, indicating that the expansion of interlayer spacing from 0.70 to 0.73 nm after K^+ extraction. Moreover, the interlayer spacing of D-MnO_2 is inconsistent with that of MnO_2-P, which indicates that the interlayer spacing variation of MnO_2-P is caused by the extraction of K-ion and the insertion of PANI. The scanning electron microscopy (SEM) images show that the pristine MnO_2 is composed of nanosheets with width ranging from 0.5 to 1 μm and the MnO_2-P displays similar morphology to the pristine MnO_2 (Figure S3, Supporting Information). The transmission electron microscopy–EDS (TEM–EDS) mapping images show the homogeneous distribution of Mn, O, and N elements over the whole nanosheet, demonstrating the existence of PANI in MnO_2-P (Figure 2c). The high-resolution TEM (HRTEM) images (Figure 2d,e) indicate that the interlayer spacing expands from 0.70 to 0.72 nm after PANI insertion, which are matched well with the result of XRD. The ICP–OES analysis (Table S1, Supporting Information) reveals that the atomic ratio of K:Mn of MnO_2 and MnO_2-P are 0.34 and 0.10, respectively, which indicates that the partial K ions are removed from the MnO_2 structure during the synthesis of MnO_2-P. Furthermore, the SEM-EDS elemental mappings (Figure S4, Supporting Information) show that the reduction of K element and the uniform distribution of N element in MnO_2-P. This results demonstrate that PANI exchange with K ion. The XPS result reveals the increase of Mn valence in MnO_2-P, which may be due to the partial removal of K^+ ions (Figure 2f). Notably, the HRTEM images show crystallized MnO_2 sheets and amorphous PANI coating with thickness

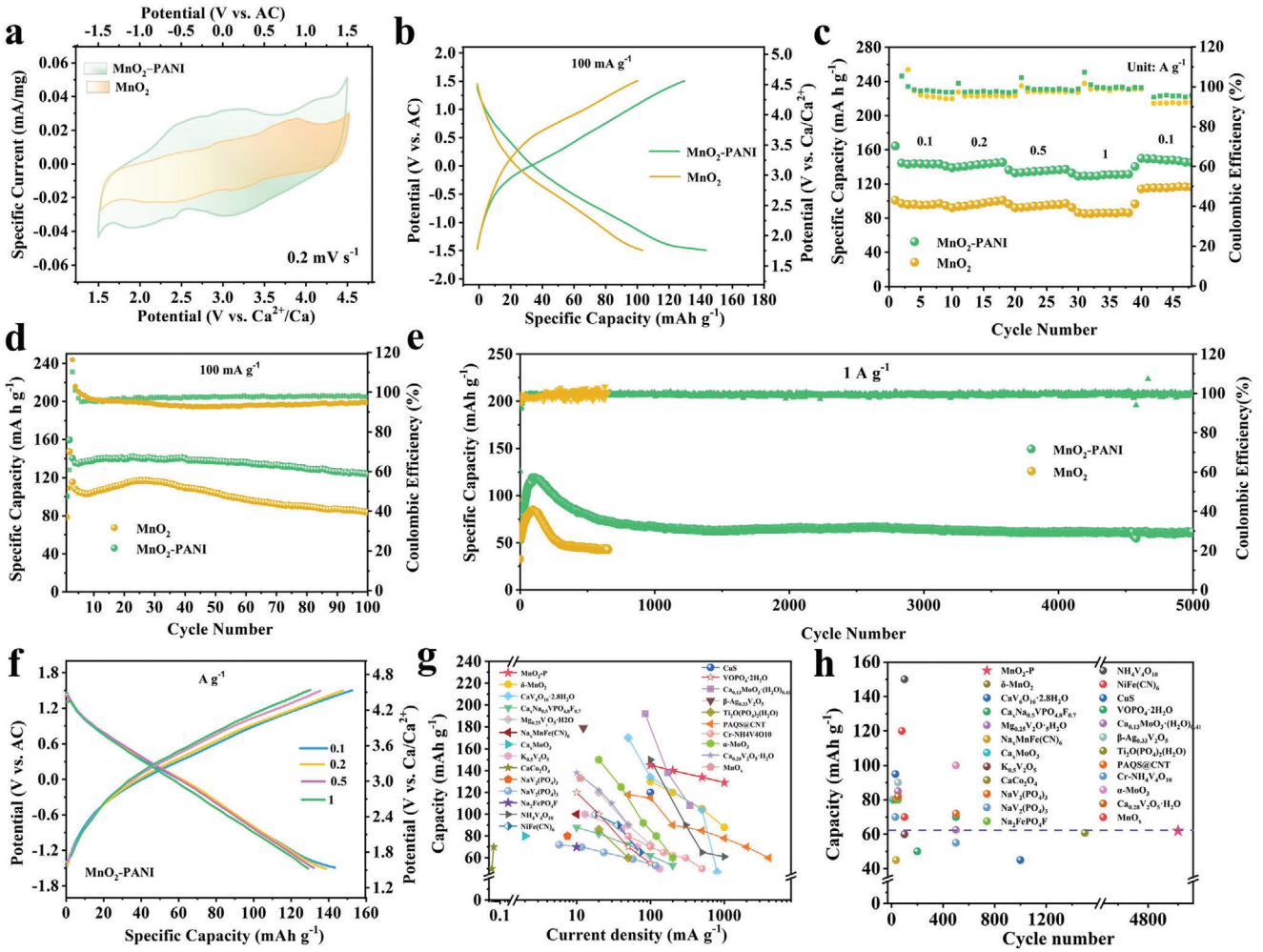

Figure 3. a) CV curves of MnO_2 and MnO_2-P. b) Corresponding GCD profiles of MnO_2 and MnO_2-P at 100 mA g^{-1}. c,d,e) Rate performance and cycling performance of MnO_2 and MnO_2-P. f) The GCD of MnO_2-P sample at different current densities. g,h) Comparison of rate capability and cycle stability.

of about 5 nm (Figure S5, Supporting Information), which indicate that the PANI coating was formed on the surface of MnO_2. In N 1s XPS spectra (Figure 2g), the peaks at 399.4 and 401.4 eV correspond to the −N = and $-N^+-$ signals, respectively, while the peak at 400.2 eV is attributed to Mn-N bond owing to the intensive interaction between MnO_2 and PANI.[8b,11] To further clarify the interaction between PANI and MnO_2 in the composite, the Fourier transform infrared (FTIR) spectroscopy and Raman spectroscopy were carried out. In the Raman spectrum of MnO_2-P, the peaks at the range of 300–700 cm^{-1} are belonged to MnO_6 groups in MnO_2,[12] and the peaks at 1100–1700 cm^{-1} are assigned to the PANI polymer.[10a] Compared to pristine MnO_2, the peak of Mn-O bond in MnO_2-P (Figure 2h) shows blue shift owing to the introduction of PANI in the composites.[13] Meanwhile, MnO_2-P exhibits a weakened $C–N^+$ stretching vibration and a low-wavenumber shift of the characteristic peaks, indicating the formation of chemical bonds (Mn-N) between MnO_2 and PANI.[14] Figure 2i demonstrates FTIR spectra of MnO_2-P, PANI and MnO_2. Compared with pure PANI, the characteristic peaks of PANI in MnO_2-P shifts to a high wavenumber owing to the existence of interactions between PANI and MnO_2.[15] In addition, the characteristic peak of MnO_2 in MnO_2 shifts toward the high wavenumber. The stronger interaction of Mn-N bond than Mn-O bond leads to the higher vibration frequency.[16] (Figure S6, Supporting Information). Besides, the FTIR spectrum of MnO_2-P also exhibits a reduction of the $C–N^+$ stretching vibration,[14] which are consistent with the Raman results. According to the result of CHNS element analysis, the PANI content of MnO_2-P sample was determined as ≈16.8 wt% (Table S2, Supporting Information). In addition, thermogravimetric analysis (TGA) curves (Figure S7) shows that the content of PANI in the MnO_2-P mixture is 17.1 wt%, which are consistent with the CHNS results. The XRD, XPS, Raman, and FTIR results all demonstrate that the MnO_2-P hybrid cathode with both PANI intercalation and coating was obtained successfully.

To further explore the benefits of organic-inorganic hybrid structure, the electrochemical test of MnO_2-P and pristine MnO_2 were evaluated in the CR2016 coin cells, in which activiated carbon (AC) as reference and counter electrodes and 0.5 M $Ca(TFSI)_2$/AN as the electrolyte. **Figure 3**a shows the cyclic voltammetry (CV) curves of MnO_2-P and pristine MnO_2 at a sweep rate of 0.2 mV s^{-1}. The MnO_2-P cathode exhibits a wider

CV area compared with MnO_2, implying a higher capacity. In particular, the first three CV curves roughly overlap, revealing a highly reversible electrochemical reaction of MnO_2-P (Figure S8, Supporting Information). The galvanostatic charge-discharge (GCD) curves of MnO_2-P and MnO_2 at the current density of 100 mA g^{-1} are displayed in Figure 3b. Significantly, the MnO_2-P shows a lower polarization potential and a higher specific capacity (150 mAh g^{-1}) than MnO_2. Moreover, the MnO_2-P provides better rate performance than that of MnO_2 (Figure 3c). The specific capacity of MnO_2-P retains 150, 140, 134, and 120 mAh g^{-1} at the current densities of 0.1, 0.2, 0.5, and 1 A g^{-1}, respectively. In addition, MnO_2-P electrode presents durable cycling stability compared to the MnO_2. Under the current density of 0.1 A g^{-1} (Figure 3d), MnO_2-P reaches higher capacity retention of 91.9% than MnO_2 (70%) after 100 cycles, exhibiting the significantly enhanced structure stability of MnO_2-P. In particular, MnO_2-P still maintains the capacity of 62 mAh g^{-1} even after 5000 cycles at 1 A g^{-1}, while the capacity of MnO_2 rapidly declines to 49 mAh g^{-1} after only 300 cycles (Figure 3e). It should be noted that the increase of capacity was observed in the first 100 cycles at the current density of 1 A g^{-1} (Figure 3e), which is ascribed to the decrease of overpotential originated from the improvement of reaction kinetics (Figure S9, Supporting Information). Moreover, the decrease of impedance after 300 cycles also proves that the increase in capacity is due to the enhancement of dynamics (Figure S10, Supporting Information). In addition, the SEM was used to characterize the morphology of MnO_2-P after cycling. The MnO_2-P after 300 cycles at 1 A g^{-1} still displays nanosheet-like morphology similar to that of the fresh one, indicating the high structural stability of MnO_2-P electrode (Figure S11, Supporting Information). As shown in the Figure S12 (Supporting Information), the (001) peak of MnO_2-P weakens after 300 cycles, indicating partial disordering during the activation of MnO_2-P. These results indicate that the capacity increase is due to the enhancement of dynamics and the activation of the electrode material. Moreover, the GCD curves of MnO_2-P cathode at various current densities display lower polarization (Figure 3f). In addition, the excellent rate performance (Figure 3g) and cycle stability (Figure 3h) of MnO_2-P cathode are superior to that of previously reported other CIBs cathode materials (Table S5, Supporting Information) .[5a,7,17]

The electrochemical kinetics of MnO_2-P and pristine MnO_2 were analyzed. **Figure 4**a shows the CV curves of MnO_2-P at different scan rates from 0.2 to 1 mV s^{-1}. As the scan rate increases, the anodic and cathodic peaks show a slight potential shift, implying a highly reversible redox reaction. The kinetic calculation details are shown in Supporting Information. The *b* values of two peaks (cathodic, anodic) were calculated to be 0.95 and 0.90, respectively (Figure 4b). These results manifest that the storage mechanism of calcium ions in MnO_2-P is dominated by capacitive process. With the increase of scanning speed from 0.2 to 1 mV s^{-1}, the capacitive capacity contribution of MnO_2-P electrode gradually increases from 70% to 86% (Figure 4c), demonstrating that the electrochemical behavior of MnO_2-P electrode is dominated by capacitive process. As shown in Figures S13 and S14 (Supporting Information), the capacitive capacity contribution of MnO_2-P (82%) is higher than that of MnO_2 (72%) for the total Ca^{2+} storage at 0.6 mV s^{-1}. Therefore, the excellent rate performance of MnO_2-P is associated with the higher contribution of capacitance behavior. In addition, the galvanostatic intermittent titration technique (GITT) test was conducted to further assess Ca^{2+} diffusion dynamics. The GITT curve of MnO_2-P electrode and the corresponding diffusion coefficients (*D*) are presented in Figure 4d. The calculation details of diffusion coefficient are shown in Figure S15 (Supporting Information). The calculation results show that the Ca–ion diffusion coefficients of MnO_2-P electrode during charge and discharge process are between $3.62 \times 10^{-10} \sim 2.51\times10^{-12}$ and $2.24\times10^{-10}\sim 3.78\times10^{-12}$ cm^2 s^{-1} (Figure 4d), respectively, which are higher than these of pristine MnO_2 (Figure S16, Supporting Information). The EIS measurements further confirm the good kinetics of MnO_2-P. As shown in Figure S17 (Supporting Information), the MnO_2-P displays a lower charge transfer resistance than pristine MnO_2, suggesting that the MnO_2-P electrode has faster interfacial charge transfer kinetics.

In addition, the diffusion paths and energy barriers of Ca^{2+} in MnO_2 and MnO_2-P were studied by climbing-image nudged elastic band (CI-NEB) calculation. The possible diffusion paths of MnO_2-P are shown in Figure S18 (Supporting Information). The calculated diffusion energy barriers of Ca-ion in MnO_2-P along *b*-axis (path 1) and *a*-axis (path 2) are 0.301 and 0.221 eV, respectively (Figure 4f), which is much lower than that of pristine MnO_2 (0.473 and 0.355 eV, respectively) (Figure 4e and Figure S19, Supporting Information). The much lower diffusion barriers for the MnO_2-P endows the Ca^{2+} transfer with fast kinetics. The electronic density of states (DOS) of pristine MnO_2 and MnO_2-P is shown in Figure 4g. Compared with the pristine MnO_2, MnO_2-P shows higher DOS intensity near Fermi energy level and noticeably narrower bandgap. This means that the introduction of PANI greatly affects the DOS and leads to a significant increase in electronic conductivity. In addition, the electronic conductivities of the electrodes were measured by four-probe method (Figure S20, Supporting Information). Consistent with the above result, the MnO_2-P electrode presents much higher electronic conductivity of 4.34 S cm^{-1} than that of the MnO_2 electrode (1.51 S cm^{-1}). In order to research the bonding behavior of Ca ions, charge density distributions of both pristine MnO_2 (Figure 4h) and MnO_2-P (Figure 4j) with one inserted Ca^{2+} were calculated. The charge transfer between Ca^{2+} and MnO_2-P is −1.46 e^-, which is lower than that between Ca^{2+} and MnO_2 (−1.79 e^-). The decreased charge transfer indicates that the less electronic interaction between the inserted Ca^{2+} ions and MnO_2 host after the introduction of polymer. The weaker electrostatic interaction between Ca^{2+} and MnO_2-P facilitates the diffusion of Ca-ion. In summary, the enhanced Ca-ion diffusivity and conductivity of MnO_2-P electrode, are responsible for the improved rate performance.

The origin of enhanced cycling stability of MnO_2-P was also studied. It is well known that manganese dissolution is the main cause for the capacity attenuation of manganese-based materials.[18] The manganese dissolution content of MnO_2 and MnO_2-P electrodes were evaluated by comparing the electrolytes before and after cycling. To observe the changes of electrolyte more clearly, the electrochemical tests were performed in a three–electrode system with the MnO_2 and MnO_2-P as working electrodes, AC and Ag/AgCl as counter electrodes and reference electrodes, respectively. Remarkably, the electrolyte for MnO_2-P still remains colorless and transparent after 300 cycles (**Figure 5**a), whereas the electrolyte for MnO_2 exhibits a significant color

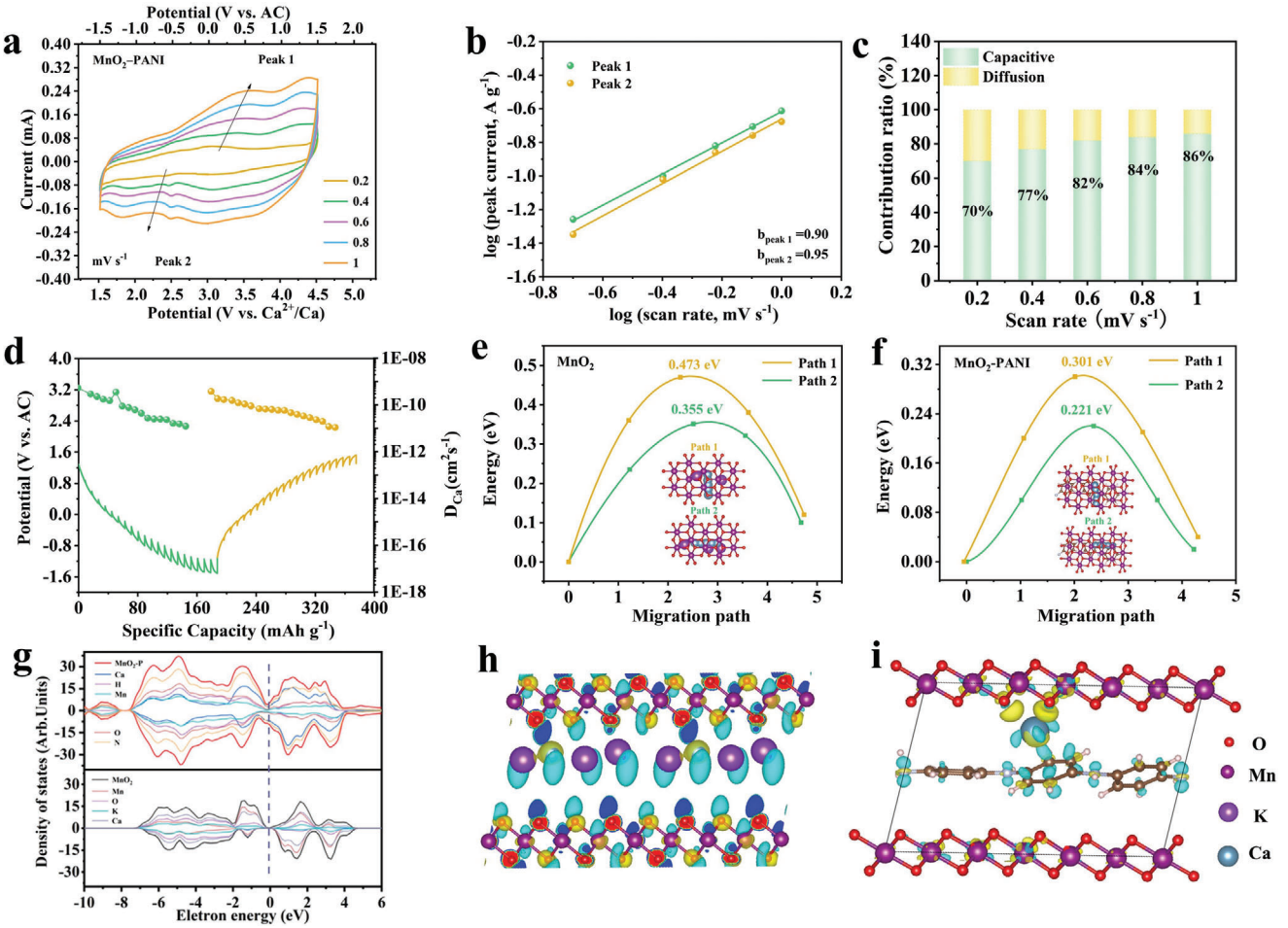

Figure 4. a) CV curves at various scan rate from 0.2 to 1.0 mV s^{-1}. b) The linear fitting curves between log *i* and log *v* of the marked peaks at different scan rates. c) The contribution ratios of the capacitive capacities in MnO_2-P electrode. d) Discharge-charge GITT profiles and the corresponding Ca^{2+} diffusion coefficient of MnO_2-P cathode. e,f) Ca^{2+} migration behaviors along the a, b-axis in MnO_2 and MnO_2-P. g) Density of states for MnO_2 and MnO_2-P, where the dashed line represents the Fermi energy at 0 eV. h,i) The differential charge density of Ca^{2+} intercalated MnO_2 and MnO_2-P. The yellow area represents charge accumulation, the light blue area represents charge depletion.

change after 100 cycles, demonstrating the dissolution of manganese species. Subsequently, the deepened yellow color of the electrolyte for MnO_2 can be easily observed after longer cycling process, indicating the dissolution of more manganese. To unveil the capacity fading mechanism of MnO_2 during cycling, the XPS analysis of the glass fiber separators and the anodes at pristine and cycled states was performed to identify the presence of Mn in electrolyte and anode after cycling. The color of glass fiber separator in MnO_2//AC cell turns dark yellow after 300 cycles (Figure S21, Supporting Information), owing to dissolving Mn^{2+} from MnO_2 electrode. In contrast, the color of the separator in the MnO_2-P//AC cell after cycling only change slightly. In the Mn 2p XPS spectrum of the pristine AC anode (Figure S22, Supporting Information), no Mn signal is detected. However, in the Mn 2p XPS spectrum of the AC anode after 300 cycles, obvious Mn 2p peaks are observed, indicating that Mn is dissolved from MnO_2 electrode and transferred to anode side. In addition, based on the ICP-OES results, the Mn element content of separator in MnO_2-P//AC cell after 300 cycles is much lower than that in MnO_2//AC cell (Figure 5b). These results demonstrate that the dissolution of MnO_2-P is effectively alleviated compared to that of MnO_2. To further study the reasons for inhibiting manganese dissolution, the DFT calculations have been applied to compute the formation energy of Mn-N bond and the energy barrier (E) of Mn atoms removed from MnO_2 and MnO_2-P. Figure S23 (Supporting Information) shows the energy change during the model optimization iteration, which indicates that demonstrating that surface Mn has been strongly fixed by Mn-N bonding. Figure 5c reveals that the escape of Mn atoms from Mn-N bonds in MnO_2-P requires an energy barrier of 5.741 eV, which is much higher than that of MnO_2 (3.862 eV). This indicates that the dissolution of manganese in MnO_2-P is more difficult than that in MnO_2. In order to explain the effect of Mn−N bond on MnO_2 electrode material, the migration of manganese in MnO_2 and MnO_2-P during Ca^{2+} de/intercalation are shown in Figure 5d. For MnO_2, the Mn dissolution into the electrolyte through the cathode/electrolyte interface in the cycling process.[19] For MnO_2-P, the dissolution of Mn on the surface is suppressed due to the formation of strong Mn-N bond between MnO_2 and PANI.

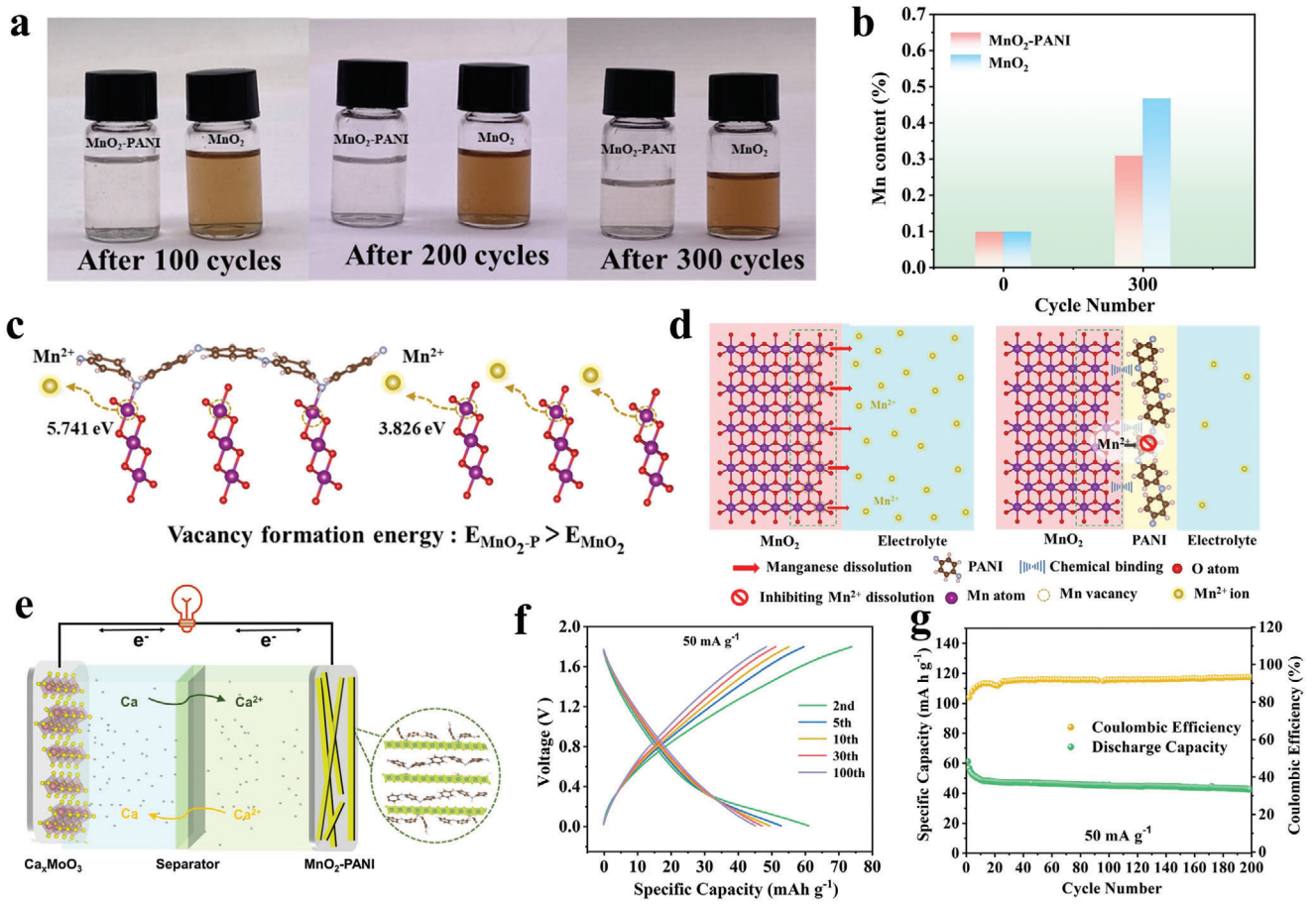

Figure 5. a) Digital images of electrolyte: after 100 cycles (left), after 200 cycles (middle) and after 300 cycles (right) in AC//MnO_2-P coin cell . b) The ICP–OES result of the glass fiber separator under different cycle number. (c) Energy barrier of manganese vacancy formation from the structure of MnO_2 and MnO_2-P. d) Mn dissolution due to the unstable or disordered surface and schematic diagram of polyaniline coating inhibiting manganese dissolution. e) Schematic structure of full CIBs. f) GCD curves and g) Cycling performance of MnO_2-P//Ca_xMoO_3 at a current density of at 50 mA g^{-1}.

In order to further prove the great potential MnO_2-P as the cathode material for CIBs, the full CIBs with MnO_2-P as cathode, $Ca(TFSI)_2$/AN as the electrolyte, and Ca_xMoO_3 as the anode were assembled. The XRD pattern in Figure S24 (Supporting Information) shows that the crystal phase of obtained anode materials is well matched with MoO_3. The SEM image shows the nanoribbons with a length of 10–15 µm and a width of 300 nm (Figure S25, Supporting Information). In addition, the charge/discharge curves of MoO_3 are shown in Figure S26 (Supporting Information). The Ca_xMoO_3 anode was formed by inserting calcium ions into MoO_3. Figure 5e demonstrates the schematic of the Ca^{2+} transfer between MnO_2-P and Ca_xMoO_3 during charge/discharge process. Both MnO_2-P and Ca_xMoO_3 electrode materials are able to realize the reversible insertion/extraction of Ca^{2+} ions. The GCD curves and cycling performance of the full CIBs are shown in Figure 5f,g, respectively. The full cell delivered a discharge capacity of 56 mA h g^{-1} at 50 mA g^{-1} and good reversibility with a capacity retention of 42 mA h g^{-1} after 200 cycles. The MnO_2-P exhibits appealing electrochemical performance in full CIBs, demonstrating its great potential for energy storage devices. To further demonstrate the great potential of MnO_2-P as the cathode material for CIBs, the Ca-metal battery with MnO_2-P as cathode, $Ca[B(hfip)_4]_2$/DME as the electrolyte, and Cametal as the anode were assembled. As shown in Figure S27 (Supporting Information), MnO_2-P shows an initial discharge capacity of 205 mAh g^{-1} at 30 mA g^{-1}. However, the discharge capacity of MnO_2-P decays to 43 mAh g^{-1} after 10 cycles (Figure S28, Supporting Information), which may be due to electrolyte instability or the passivation of the metal Ca surface[20]

To reveal the Ca^{2+} ion storage mechanism of the MnO_2-P, in situ XRD and ex situ characterizations were carried out. **Figure 6**a shows the in situ XRD patterns and the corresponding GCD curves of MnO_2-P. Figure S29 (Supporting Information) shows that the (001) peak intensity of MnO_2-P decreases gradually during discharge, indicating that MnO_2-P changes into a disordered structure during Ca^{2+} insertion. The diffraction peak is partially irreversible disordering after extracting Ca^{2+}. In the ex situ XRD pattern of MnO_2-P (Figure S30, Supporting Information), irreversible disordering occurs in the first cycle, but a reversible transformation of the ordered and disordered structure occurs in subsequent cycles. This is consistent with the previously reported mechanism of calcium ion insertion/extraction in manganese dioxide. In view of the in/ex situ XRD results, the interlayer

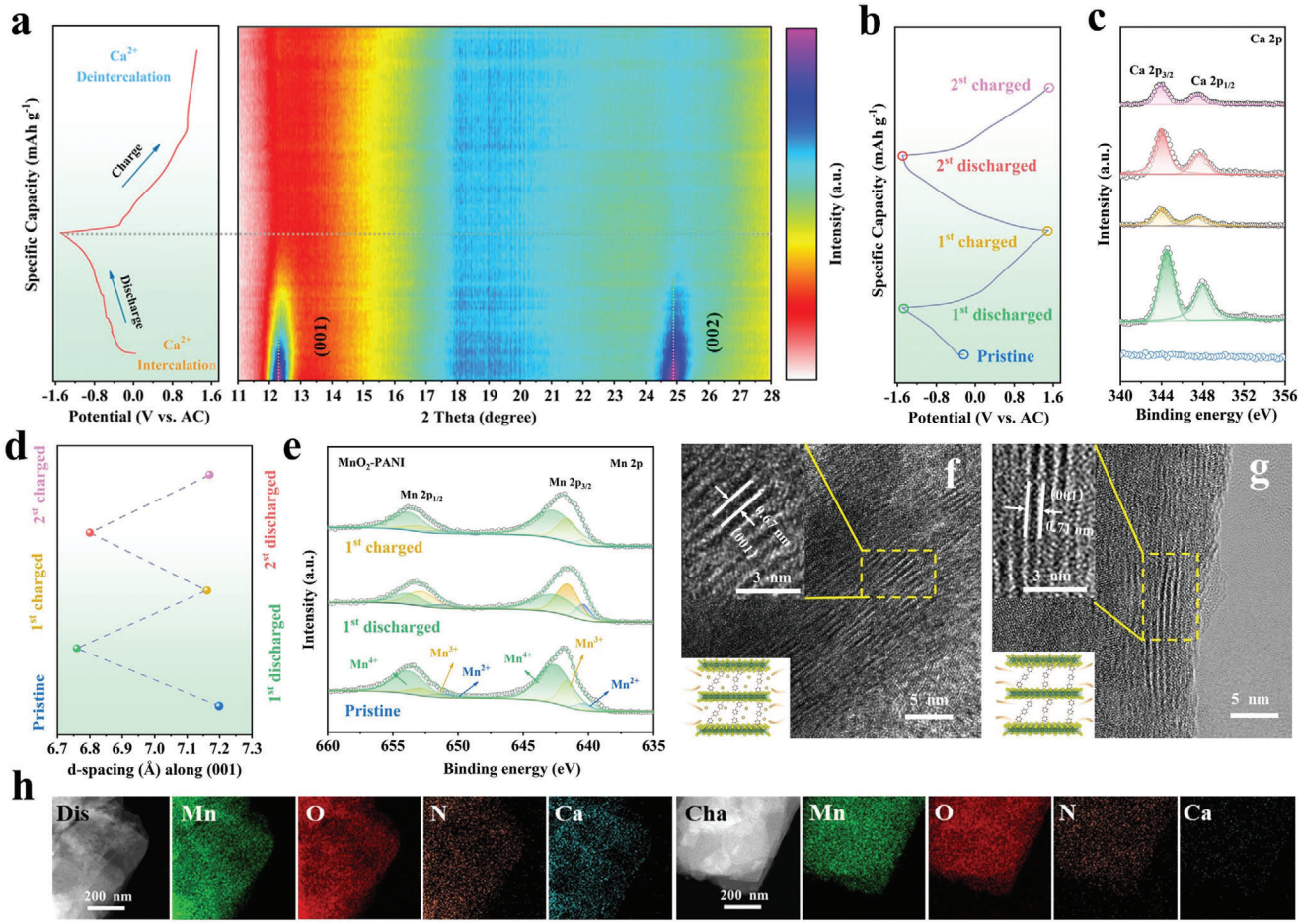

Figure 6. a) In situ XRD patterns and b) the GCD profiles of MnO_2-P. c) Ca 2p XPS spectra of MnO_2-P and d) (001) d-spacings of MnO_2-P at pristine (blue colored), 1st discharged (green colored), 1st charged (orange colored), 2nd discharged (red colored) and 2nd charged states (pink colored). e) Mn 2p XPS spectra of MnO_2-P at the pristine, discharged and charged states. f,g) HRTEM images of MnO_2-P and h) STEM-EDS mapping images at the discharged and charged states.

spacing of the MnO_2-P in different states were compared (Figure 6d). In the discharge state, the characteristic peak (001) shifts from 12.2° to 13.0°, implying the decrease of d-spacing from 0.72 to 0.67 nm. This contraction of interlayer spacing can be attributed to the attraction force between intercalated Ca^{2+} and the oxygen layer of MnO_2.[17m] Subsequently, upon the first charge (Figure S30, Supporting Information), the (110) peak recovers to the original state, the d-spacing increased from 0.67 to 0.72 nm, demonstrating a good reversibility of MnO_2-P cathode. Figure 6c shows the high-resolution Ca 2p XPS spectra of MnO_2-P at different states. In the pristine state, the Ca 2p XPS spectrum exhibit the absence of calcium. Upon discharging to −1.5 V (vs AC), strong Ca 2p signals were detected, while the intensity significantly decreased after charging to 1.5 V. Figure 6e shows the Mn 2p XPS spectra of MnO_2-P at different states. In the discharged MnO_2-P electrode, the intensity of Mn^{4+} peak at 642.6 eV weakens while that of Mn^{3+} peak at 641.7 eV enhances, implying the reduction of Mn^{4+} to Mn^{3+} during the insertion of Ca^{2+}. Correspondingly, the intensity of the Mn^{4+} peak increases after charging, which demonstrates that the Mn^{3+} is oxidized to Mn^{4+} during the charging process (Table S4, Supporting Information).

To determine whether PANI also undergo redox reactions during electrochemical charge/discharge, ex situ N 1s XPS analysis (Figure S31, Supporting Information) was performed. The N 1s XPS spectra of pristine MnO_2-P cathode were fitted with three peaks related to benzoid amine −NH−, quinoid imine −N = , and positively charged nitrogen $-N^+-$, located at 400.2, 399.4, and 401.4 eV, respectively.[21] The peak intensity of −N = at 399.4 eV is strengthened at discharged state and weakened at charged state, indicating the conversion between the quinonoid rings and benzenoid rings during the charge/discharge.[22] These results demonstrate that the redox reaction of polyaniline also occurs during electrochemical charge/discharge. Moreover, the Ca/Mn atomic ratios of MnO_2-P at the pristine, 1st discharged, 1st charged states were determined to be 0.00, 0.44, and 0.03, respectively, demonstrating the reversible Ca^{2+} insertion/extraction in MnO_2-P (Table S3, Supporting Information). In addition, the ex situ HRTEM images further reveal that the interlayer distances of the fully discharged and charged of MnO_2-P are 0.67 and 0.72 nm (Figure 6f,g), respectively, which agree well with the in/ex situ XRD results. The EDS mappings of the discharged MnO_2-P reveal the clear outlines of Mn, O, N, and Ca elements, which

confirms the Ca^{2+} intercalation (Figure 6h). Upon charging to 1.5 V, the weak Ca signal indicates the Ca^{2+} deintercalation. These results confirm the (de)intercalation mechanism of Ca^{2+} in MnO_2-P is a single-phase solid solution reaction.

3. Conclusions

In summary, we design high-performance MnO_2-P cathode with both PANI intercalation and coating for CIBs. Detailed characterization combined with experiments strongly demonstrate the successful intercalation of PANI in the MnO_2 layer and the formation of Mn-N bond on the surface of MnO_2. The intercalated PANI in MnO_2 expands layer spacing and achieves the better rate performance than pristine MnO_2. The electron delocalization on the PANI weaken local charge transfer for facilitating Ca^{2+} diffusion. Moreover, the PANI coating suppresses the dissolution of Mn by forming Mn-N bond thus enhances structural stability. A combination of kinetic analysis and DFT results reveal that the organic-inorganic hybrid materials (MnO_2-P) had faster ion transport kinetics and inhibit the dissolution of Mn. Hence, MnO_2-P exhibits superior rate capability (120 mAh g^{-1} at 1 A g^{-1}) and long-term cycle (62 mAh g^{-1} over 5000 cycles), which is superior to previous reported other CIBs cathodes materials. This work provides a novel roadmap to explore or engineer cathode materials for advanced CIBs.

Supporting Information

Supporting Information is available from the Wiley Online Library or from the author.

Acknowledgements

This work was supported by the National Natural Science Foundation of China (52172231, 51972259, 52202290 and 52102300), the Natural Science Foundation of Hubei Province (2022CFA087), Industrialization Project of Xiangyang Technology Transfer Center of Wuhan University of Technology (WXCJ-20220017).

Conflict of Interest

The authors declare no conflict of interest.

Data Availability Statement

The data that support the findings of this study are available from the corresponding author upon reasonable request.

Keywords

cathode materials, manganese oxide, Mn dissolution, polyaniline, rechargeable Ca-ion batteries

Received: April 4, 2023
Revised: May 28, 2023
Published online:

[1] a) K. Kang, Y. S. Meng, J. Breger, C. P. Grey, G. Ceder, *Science* **2006**, *311*, 977; b) M. Li, Y. Zhang, J. Hu, X. Wang, J. Zhu, C. Niu, C. Han, L. Mai, *Nano Energy* **2022**, *100*, 107539; c) M. Wang, C. Jiang, S. Zhang, X. Song, Y. Tang, H.-M. Cheng, *Nat. Chem.* **2018**, *10*, 667.
[2] a) M. Li, J. Lu, X. Ji, Y. Li, Y. Shao, Z. Chen, C. Zhong, K. Amine, *Nat. Rev. Mater.* **2020**, *5*, 276; b) X. Zhang, D. Li, Q. Ruan, L. Liu, B. Wang, F. Xiong, C. Huang, P. K. Chu, *Mater. Today Energy* **2023**, *32*, 101232.
[3] D.-J. Yoo, M. Heeney, F. Glocklhofer, *Nat. Commun.* **2021**, *12*, 2386.
[4] X. Xu, M. Duan, Y. Yue, Q. Li, X. Zhang, L. Wu, P. Wu, B. Song, L. Mai, *ACS Energy Lett.* **2021**, *6*, 1560.
[5] a) S. Zhang, Y. Zhu, D. Wang, C. Li, Y. Han, Z. Shi, S. Feng, *Adv. Sci.* **2022**, *9*, 2200397; b) T. Chen, G. Sai Gautam, P. Canepa, *Chem. Mater.* **2019**, *31*, 8087.
[6] a) D. Chao, W. Zhou, C. Ye, Q. Zhang, Y. Chen, L. Gu, K. Davey, S.-Z. Qiao, *Angew. Chem. Int. Ed. Engl.* **2019**, *58*, 7823; b) G. Li, W. Chen, H. Zhang, Y. Gong, F. Shi, J. Wang, R. Zhang, G. Chen, Y. Jin, T. Wu, Z. Tang, Y. Cui, *Adv. Energy Mater.* **2020**, *10*, 1902085; c) B. Sambandam, V. Mathew, S. Kim, S. Lee, S. Kim, J. Y. Hwang, H. J. Fan, J. Kim, *Chem* **2022**, *8*, 924.
[7] C. Zuo, F. Xiong, J. Wang, Y. An, L. Zhang, Q. An, *Adv. Funct. Mater.* **2022**, *32*, 2202975.
[8] a) J. Heo, S. Chong, S. Kim, R. Kim, K. Shin, J. Kim, H. T. Kim, *Batteries Supercaps* **2021**, *4*, 1881; b) J. Huang, X. Tang, K. Liu, G. Fang, Z. He, Z. Li, *Mater. Today Energy* **2020**, *17*, 100475.
[9] a) J. Huang, Z. Wang, M. Hou, X. Dong, Y. Liu, Y. Wang, Y. Xia, *Nat. Commun.* **2018**, *9*, 4383; b) W. Sun, F. Wang, S. Hou, C. Yang, X. Fan, Z. Ma, T. Gao, F. Han, R. Hu, M. Zhu, *J. Am. Chem. Soc.* **2017**, *139*, 9775.
[10] a) W. Li, C. Han, Q. Gu, S. L. Chou, J. Z. Wang, H. K. Liu, S. X. Dou, *Adv. Energy Mater.* **2020**, *10*, 2001852; b) E. Pomerantseva, Y. Gogotsi, *Nat. Energy* **2017**, *2*, 17089; c) P. Xiong, B. Sun, N. Sakai, R. Ma, T. Sasaki, S. Wang, J. Zhang, G. Wang, *Adv. Mater.* **2020**, *32*, 1902654.
[11] a) S. Chen, K. Li, K. S. Hui, J. Zhang, *Adv. Funct. Mater.* **2020**, *30*, 2003890; b) Y. Zhao, R. Zhou, Z. Song, X. Zhang, T. Zhang, A. Zhou, F. Wu, R. Chen, L. Li, *Angew Chem Int Edit* **2022**, *61*, e202212231.
[12] Q. Xie, G. Cheng, T. Xue, L. Huang, S. Chen, Y. Sun, M. Sun, H. Wang, L. Yu, *Mater Today Energy* **2022**, *24*, 100934.
[13] X. Zheng, J. Cai, Y. Cao, L. Shen, Y. Zheng, F. Liu, S. Liang, Y. Xiao, L. Jiang, *Applied Appl Catal B-Environ* **2021**, *297*, 120402.
[14] Y. Chen, Y. Xie, *Adv. Electron. Mater.* **2019**, *5*, 1900816.
[15] P. Asen, S. Shahrokhian, A. I. Zad, *J Solid State Electr* **2018**, *22*, 983.
[16] a) M. K. Bharty, A. Bharti, R. Chaurasia, U. K. Chaudhari, S. K. Kushawaha, P. K. Sonkar, V. Ganesan, R. J. Butcher, *Polyhedron* **2019**, 173; b) L. Zhang, S.-Y. Niu, J. Jin, L.-P. Sun, G.-D. Yang, L. Ye, *Inorg. Chim. Acta* **2009**, *362*, 1448.
[17] a) M. S. Chae, H. H. Kwak, S.-T. Hong, *ACS Appl Energy Mater* **2020**, *3*, 5107; b) M. E. Purbarani, J. Hyoung, S.-T. Hong, *ACS Appl Energy Mater* **2021**, *4*, 7487; c) W. Ren, F. Xiong, Y. Fan, Y. Xiong, Z. Jian, *ACS Appl. Mater. Interfaces* **2020**, *12*, 10471; d) X. Xu, M. Duan, Y. Yue, Q. Li, X. Zhang, L. Wu, P. Wu, B. Song, L. Mai, *ACS Energy Lett.* **2019**, *4*, 1328; e) J. Wang, J. Wang, Y. Jiang, F. Xiong, S. Tan, F. Qiao, J. Chen, Q. An, L. Mai, *Adv. Funct. Mater.* **2022**, 32; f) B. Jeon, H. H. Kwak, S.-T. Hong, *Chem. Mater.* **2022**, *34*, 1491; g) B. J. Kwon, L. Yin, C. J. Bartel, K. Kumar, P. Parajuli, J. Gim, S. Kim, Y. A. Wu, R. F. Klie, S. H. Lapidus, B. Key, G. Ceder, J. Cabana, *Chem. Mater.* **2022**, *34*, 836; h) A. L. Lipson, B. Pan, S. H. Lapidus, C. Liao, J. T. Vaughey, B. J. Ingram, *Chem. Mater.* **2015**, *27*, 8442; i) M. Cabello, F. Nacimiento, J. R. Gonzalez, G. Ortiz, R. Alcantara, P. Lavela, C. Perez-Vicente, J. L. Tirado, *Electrochem. Commun.* **2016**, *67*, 59; j) S. J. R. Prabakar, W.-B. Park, J. Y. Seo, S. P. Singh, D. Ahn, K.-S. Sohn, M. Pyo, *Energy Storage Mater.* **2021**, *43*, 85; k) J. Hyoung, J. W. Heo, B. Jeon, S.-T. Hong, *J. Mater. Chem. A* **2021**, *9*, 20776; l) M. Adil, A. Sarkar, S. Sau, D. Muthuraj, S. Mitra, *J. Power Sources* **2022**, 541; m) J. Hyoung, J. W.

Heo, S.-T. Hong, *J. Power Sources* **2018**, *390*, 127; n) N. Kuperman, P. Padigi, G. Goncher, D. Evans, J. Thiebes, R. Solanki, *J. Power Sources* **2017**, *342*, 414; o) S. Kim, L. Yin, S. M. Bak, T. T. Fister, H. Park, P. Parajuli, J. Gim, Z. Yang, R. F. Klie, P. Zapol, Y. Du, S. H. Lapidus, J. T. Vaughey, *Nano Lett.* **2022**, *22*, 2228.

[18] T. Xiong, Y. Zhang, W. S. V. Lee, J. Xue, *Adv. Energy Mater.* **2020**, 10.

[19] a) J. Lu, C. Zhan, T. Wu, J. Wen, Y. Lei, A. J. Kropf, H. Wu, D. J. Miller, J. W. Elam, Y.-K. Sun, *Nat. Commun.* **2014**, *5*, 5693; b) C. Zhan, J. Lu, A. Jeremy Kropf, T. Wu, A. N. Jansen, Y.-K. Sun, X. Qiu, K. Amine, *Nat. Commun.* **2013**, *4*, 2437.

[20] a) Z. Li, B. P. Vinayan, P. Jankowski, C. Njel, A. Roy, T. Vegge, J. Maibach, J. M. G. a. Lastra, M. Fichtner, Z. ZhaoKarger, *Angew Chem Int Edit* **2020**, *59*, 11483; b) Z.-L. Xu, J. Park, J. Wang, H. Moon, G. Yoon, J. Lim, Y.-J. Ko, S.-P. Cho, S.-Y. Lee, K. Kang, *Nat. Commun.* **2021**, *12*, 3369.

[21] P. Luo, Y. Xiao, J. Yang, C. Zuo, F. Xiong, C. Tang, G. Liu, W. Zhang, W. Tang, S. Wang, S. Dong, Q. An, *Chem. Eng. J.* **2022**, *433*, 133772.

[22] a) Z. Zhao, T. Yu, Y. Miao, X. Zhao, *Electrochim. Acta* **2018**, *270*, 30; b) S. Chen, K. Li, K. S. Hui, J. Zhang, *Adv. Funct. Mater.* **2020**, *30*, 2003890.